

# Reconstruction of the SNO+ Experiment

Jie Hu

A Dissertation

Presented to the Faculty  
of University of Alberta  
in Candidacy for the Degree  
of Doctor of Philosophy

Recommended for Acceptance  
by the Department of  
Department of Physics

January, 2019

© Copyright 2019 by Jie Hu.

All rights reserved.

# Abstract

## 0.1 Abstract

A neutrino is one of the elementary particles we currently know and is included in the Standard Model (SM). However, some properties of neutrinos can not be described by the SM, which shows clues of the new physics beyond the Standard Model.

SNO+ experiment is planned to explore one of the unknown properties of neutrinos : whether the neutrinos are Majorana particles or Dirac particles.

# Acknowledgements

# Table des matières

<b>Abstract</b>	<b>iii</b>
0.1 Abstract . . . . .	iii
<b>Acknowledgements</b>	<b>iv</b>
<b>Table des matières</b>	<b>v</b>
<b>Table des figures</b>	<b>viii</b>
<b>Liste des tableaux</b>	<b>ix</b>
<b>1 Introduction</b>	<b>1</b>
1.1 Studies on Solar Neutrinos : History and Current Status . . . . .	1
<b>2 Neutrino physics</b>	<b>2</b>
2.1 Neutrino Flavor Transformation and Oscillation . . . . .	2
2.1.1 Vacuum Oscillation . . . . .	2
2.1.2 Matter Effect . . . . .	2
2.1.3 Three-flavor Mixing . . . . .	4
2.1.4 Reactor-solar Experiments . . . . .	6
2.1.5 Atmosphere-accelerator Experiments . . . . .	6
2.1.6 Astrophysics Experiments . . . . .	6
2.2 Majorana Neutrino . . . . .	6

2.3	Double Beta Decay . . . . .	7
2.3.1	Status of Double Beta Decay Experiments . . . . .	8
<b>3</b>	<b>The SNO+ Experiment</b>	<b>11</b>
3.1	A Description of SNO+ Detector . . . . .	11
3.1.1	Overview . . . . .	11
3.1.2	SNO+ Physics Phases . . . . .	12
3.1.3	Detection Principle . . . . .	13
3.1.4	Electronics . . . . .	14
3.1.5	Optics . . . . .	15
3.1.6	Liquid scintillator . . . . .	15
3.1.7	Calibration . . . . .	17
<b>4</b>	<b>Event Reconstruction</b>	<b>19</b>
4.1	Reconstruction of the SNO+ . . . . .	19
4.2	Reconstruction Algorithms for Position, Time and Energy of Events in SNO+ . . . . .	19
4.3	An Alternative Vertex Reconstruction Algorithm for SNO+ . . . . .	19
4.4	Likelihood Calculation . . . . .	25
4.5	$^{16}\text{N}$ test . . . . .	26
4.6	Vertex Reconstruction for the SNO+ Partial-phase . . . . .	27
4.7	PMT Selectors . . . . .	32
4.8	$^{16}\text{N}$ Calibration . . . . .	32
4.8.1	Water Phase Calibration . . . . .	33
4.8.2	Partial-fill Phase Calibration . . . . .	33
<b>5</b>	<b>Partial-filled Scintillator Phase</b>	<b>34</b>
<b>6</b>	<b>Conclusions</b>	<b>37</b>
<b>A</b>	<b>Appendix Name</b>	<b>38</b>



# Table des figures

3.1	A Jablonski diagram for the liquid scintillator, modified from [16, 5]. . . . .	16
4.1	PMT response time as the timing pdf. . . . .	21
4.2	PMT angular distribution as the angular response pdf. . . . .	21
4.3	Likelihood surface of an $^{16}\text{N}$ event projected on X-Y, Y-Z, X-Z planes. A clear global maxima is reached for the fitted vertex. . . . .	28
4.4	Likelihood surface of an $^{16}\text{N}$ event projected on x, y, z, t axes. . . . .	29
4.5	Derivatives of logLikelihood of an $^{16}\text{N}$ event projected on x, y, z, t axes. The analytical derivatives (blue) are overlaid with numerical derivatives. . . . .	29



# Liste des tableaux

2.1	Oscillation neutrino experiments. . . . .	5
4.1	Position resolution parameters for the MP Water Fitter. . . . .	27
4.2	scintillator $\alpha/\beta$ timing parameters??. . . . .	31

# Chapitre 1

## Introduction

Neutrinos are one of the elementary particles we currently know and are included in the Standard Model (SM). However, some properties of neutrinos can not be described by the SM, which shows clues of the new physics beyond the SM.

SNO+ is a multi-purpose neutrino experiment

SNO+ experiment is planned to explore one of the unknown properties of neutrinos : whether the neutrinos are Majorana particles or Dirac particles.

In this thesis, a position and time reconstruction algorithm is developed for SNO+ physics phases.

calibration

solar neutrino and backgrounds analysis

the SNO+ water phase and partial scintillator fill phase.

### 1.1 Studies on Solar Neutrinos : History and Current Status

## Chapitre 2

# Neutrino physics

### 2.1 Neutrino Flavor Transformation and Oscillation

Neutrino oscillation was first discovered in 1998. It is the first direct evidence showing that the Standard Model is incomplete.

The neutrinos generated with definite flavor from weak interactions and related to solar neutrino oscillations

#### 2.1.1 Vacuum Oscillation

#### 2.1.2 Matter Effect

The matter effect is caused by neutrinos interacting with ambient electrons and nucleons in matter such as the Sun or the Earth.  $\nu_e$  interacts with electrons via both charged weak current (exchanging  $W$  boson) and neutral weak current ( $Z$  boson) while  $\nu_\mu$  and  $\nu_\tau$  interact only by the neutral current. The  $\nu_e$  energy has an addition term,  $V_{CC} = \sqrt{2}G_F n_e$ , where  $n_e$  is the number density of the electrons in matter and  $G_F$  is the Fermi coupling constant for the weak interaction. This affects the oscillation probabilities for neutrinos propagating in matter compared to vacuum, which is called the Mikheyev-Smirnov-Wolfenstein (MSW) mechanism[24, 23].

In vacuum two-flavor mixing, the Schrödinger equation can be written (in natural

units)[28] :

$$i \frac{d}{dt} \begin{bmatrix} \nu_e \\ \nu_\mu \end{bmatrix} = H_0^f \begin{bmatrix} \nu_e \\ \nu_\mu \end{bmatrix}, \quad (2.1)$$

where

$$H_0^f = \frac{1}{2E} \begin{bmatrix} m_1^2 \cos^2 \theta + m_2^2 \sin^2 \theta & (m_2^2 - m_1^2) \sin \theta \cos \theta \\ (m_2^2 - m_1^2) \sin \theta \cos \theta & m_1^2 \sin^2 \theta + m_2^2 \cos^2 \theta \end{bmatrix} = \frac{\Delta m_{21}^2}{4E} \begin{bmatrix} -\cos 2\theta & \sin 2\theta \\ \sin 2\theta & \cos 2\theta \end{bmatrix} + \frac{(m_1^2 + m_2^2)}{4E} \begin{bmatrix} 1 & 0 \\ 0 & 1 \end{bmatrix}, \quad (2.2)$$

and  $\Delta m_{21}^2 = (m_2^2 - m_1^2)$ .

To simplify the calculation, we can drop the second unitary term of  $H_0^f$  that is irrelevant to the neutrino flavor transformation. Including the matter effect, we obtain :

$$H_m = \begin{bmatrix} -\frac{\Delta m_{21}^2}{4E} \cos 2\theta + \sqrt{2} G_F n_e & \frac{\Delta m_{21}^2}{4E} \sin 2\theta \\ \frac{\Delta m_{21}^2}{4E} \sin 2\theta & \frac{\Delta m_{21}^2}{4E} \cos 2\theta \end{bmatrix} \quad (2.3)$$

We define a mixing angle in matter,  $\theta_m$  as :

$$\tan 2\theta_m = \frac{\Delta m^2 \sin 2\theta}{\Delta m^2 \cos 2\theta - 2\sqrt{2} E G_F n_e}, \quad (2.4)$$

and define an effective squared-mass difference in matter  $\Delta m_m^2$  as :

$$\Delta m_m^2 = \sqrt{(\Delta m^2 \cos 2\theta - 2\sqrt{2} E G_F n_e)^2 + (\Delta m^2 \sin 2\theta)^2}. \quad (2.5)$$

In analogy with mixing in vacuum, we can write the mixing equation relating the energy eigenstates in matter ( $\nu_{1m}, \nu_{2m}$ ) to the flavor eigenstates with a diagonalized Hamiltonian :

$$\begin{bmatrix} \nu_e \\ \nu_\mu \end{bmatrix} = \begin{bmatrix} \cos \theta_m & \sin \theta_m \\ -\sin \theta_m & \cos \theta_m \end{bmatrix} \begin{bmatrix} \nu_{1m} \\ \nu_{2m} \end{bmatrix}. \quad (2.6)$$

The probability of flavor transformation in matter is :

$$P_{\nu_e \rightarrow \nu_\mu} = \sin^2(2\theta_m) \sin^2\left(\frac{\Delta m_m^2 L}{4E}\right). \quad (2.7)$$

The denominator in equation (2.4) implies a resonance condition :

$$V(n_e) = \sqrt{2}G_F n_e = \frac{\Delta m^2 \cos 2\theta}{2E}. \quad (2.8)$$

From this condition, for a given  $E$ , there is a resonance density  $n_e^{reson}$  while for a given  $n_e$ , there is a resonance energy  $E^{reson}$ . When the resonance condition is satisfied,  $\theta_m = \frac{\pi}{4}$  and two flavor neutrinos are maximally mixed, even if the vacuum mixing angle  $\theta$  is small. This is called matter enhanced neutrino oscillation[24, 10].

### 2.1.3 Three-flavor Mixing

For three-flavor neutrino mixing, we have[25] :

$$|\nu_f\rangle = \sum_{k=1}^3 U_{fk}^* |\nu_k\rangle, \quad (2.9)$$

where  $f = e, \mu, \tau$  and  $k = 1, 2, 3$ . The unitary PMNS matrix,  $U_{PMNS}$ , can be parametrized as :

$$U_{PMNS} = \begin{bmatrix} 1 & 0 & 0 \\ 0 & \cos \theta_{23} & \sin \theta_{23} \\ 0 & -\sin \theta_{23} & \cos \theta_{23} \end{bmatrix} \begin{bmatrix} \cos \theta_{13} & 0 & e^{-i\delta_{CP}} \sin \theta_{13} \\ 0 & 1 & 0 \\ e^{-i\delta_{CP}} \sin \theta_{13} & 0 & \cos \theta_{13} \end{bmatrix} \begin{bmatrix} \cos \theta_{12} & \sin \theta_{12} & 0 \\ -\sin \theta_{12} & \cos \theta_{12} & 0 \\ 0 & 0 & 1 \end{bmatrix}. \quad (2.10)$$

In the PMNS matrix, we have four parameters : the three mixing angles  $\theta_{12}$ ,  $\theta_{13}$ ,  $\theta_{23}$  and the charge-parity (CP) violation parameter of lepton sector,  $\delta_{CP}$ . The unknown value of  $\delta_{CP}$  is related to leptogenesis, the hypothetical physical process that produced an asymmetry between leptons and antileptons in the very early universe[?]. In addition, there are two squared-mass differences,  $\Delta m_{21}^2 = m_2^2 - m_1^2$  and  $\Delta m_{32}^2 = |m_3^2 - m_2^2|$ . The sign of  $\Delta m_{32}^2$  is unknown and it indicates a mass hierarchy problem of whether neutrino mass is normal hierarchy (NH,  $m_3 > m_2 > m_1$ ) or inverted hierarchy (IH,  $m_3 < m_1 < m_2$ )[25].

Currently, these six parameters have been measured by neutrino oscillation experiments. These experiments can be classified by the neutrino sources they use. They are the solar, the reactor, the atmospheric, the accelerator and the astronomical neutrino experiments. Table 2.1 lists the energy scale of the neutrino source as well as the example experiments.

TABLE 2.1 – Oscillation neutrino experiments.

type	source	$E_\nu$	example
solar	the Sun	MeV scale	SNO
reactor	reactor	MeV scale	DayaBay
atmospheric	cosmic-ray	GeV scale	SuperK
accelerator	$\nu$ beam from accelerator	GeV scale	T2K
astronomical	astronomical objects	GeV-EeV scale	IceCube

For the  $\Delta m_{21}^2$  and  $\theta_{12}$ , the combined analysis of the measurements from the reactor experiment KamLAND and SNO gave  $\Delta m_{21}^2 = 7.59_{-0.21}^{+0.21} \times 10^{-5} eV^2$  and  $\tan^2 \theta_{21} = 0.47_{-0.05}^{+0.06} [?]$ .

The accelerator neutrino experiments as well as the atmospheric neutrino experiments have measured  $\Delta m_{32}^2$  and  $\theta_{23}$ . The most recent results from SuperK show that in NH,  $\sin^2 \theta_{23} = 0.588_{-0.064}^{+0.031}$  and  $\Delta m_{32}^2 = 2.5_{-0.20}^{+0.13} \times 10^{-3} eV^2 [?]$ .

In 2012, the reactor neutrino experiment Daya Bay reported the discovery of non-zero  $\theta_{13}$  with a significance of  $5.2\sigma$ . In 2016, Daya Bay reported that  $\sin^2 2\theta_{13} = 0.0841 \pm 0.0027(stat.) \pm 0.0019(syst.)$ . This high-precision result makes  $\sin^2 2\theta_{13}$  the best measured mixing angle[?, ?].

$\delta_{CP}$  is examined by the experiments which measure the difference between neutrino and antineutrino oscillation probabilities  $P(\bar{\nu}_\alpha \rightarrow \bar{\nu}_\beta)$  and  $P(\nu_\alpha \rightarrow \nu_\beta)[?]$ . In 2017, the T2K experiment in Japan rejected the hypothesis that neutrinos and antineutrinos oscillate with the same probability at 95% confidence ( $2\sigma$ ) level. This indicates a hint of CP symmetry broken by neutrinos[?].

The oscillation probability in matter can be written in a concise and exact form as [15] :

$$P(\nu_e \rightarrow \nu_\mu) = A \cos \delta + B \sin \delta + C$$

will also provide the information for the CP- and T-violation by investigating the quantities of :

$$A_{CP} = \frac{P(\nu_\alpha \rightarrow \nu_\beta) - P(\bar{\nu}_\alpha \rightarrow \bar{\nu}_\beta)}{P(\nu_\alpha \rightarrow \nu_\beta) + P(\bar{\nu}_\alpha \rightarrow \bar{\nu}_\beta)}$$

$$A_T = \frac{P(\nu_\alpha \rightarrow \nu_\beta) - P(\bar{\nu}_\beta \rightarrow \bar{\nu}_\alpha)}{P(\nu_\alpha \rightarrow \nu_\beta) + P(\bar{\nu}_\beta \rightarrow \bar{\nu}_\alpha)}$$

### 2.1.4 Reactor-solar Experiments

KamLand

Daya Bay

The Jiangmen Underground Neutrino Observatory (JUNO) is a reactor neutrino experiment located at Kaiping, Jiangmen in Southern China. a large liquid scintillator detector large active mass of 20 kton

the energy resolution (3% at 1 MeV) [11]

### 2.1.5 Atmosphere-accelerator Experiments

### 2.1.6 Astrophysics Experiments

Neutrino telescopes Ice cube Baikal

## 2.2 Majorana Neutrino

Dirac equation  $(i\gamma^\mu\partial_\mu - m)\psi = 0$ , get coupled equations

The interpretation of the  $0\nu\beta\beta$  process is considered as exchanging light Majorana neutrinos. In this case the effective Majorana mass  $\langle m_{ee} \rangle = \sum_{i=1}^3 |U_{ei}|^2 m_i$  ( $i = 1, 2, 3$ ), where  $U_{ei}$  are the elements of the neutrino mixing matrix for the flavor state  $\nu_e$ , and  $m_i$  are the mass eigenvalues of the mass eigenstates (from (2.9)). The observable quantity is the half-life :

$$(T_{1/2}^{0\nu\beta\beta})^{-1} = G_{PS}(Q, Z) |M_{Nuclear}|^2 \langle m_{ee} \rangle^2,$$

Majorana found a representation of the  $\gamma$ -matrices as follow :

$$\gamma_M^0 = \begin{pmatrix} 0 & \sigma^2 \\ \sigma^2 & 0 \end{pmatrix}, \gamma_M^1 = \begin{pmatrix} \sigma^3 & 0 \\ 0 & \sigma^3 \end{pmatrix}, \gamma_M^2 = \begin{pmatrix} -\sigma^2 & 0 \\ 0 & \sigma^2 \end{pmatrix}, \gamma_M^3 = -i \begin{pmatrix} \sigma^1 & 0 \\ 0 & \sigma^1 \end{pmatrix}$$

These matrices themselves are pure imaginary.

## 2.3 Double Beta Decay

For heavy radioactive isotopes with nuclei of even neutron number (N) and even proton number (Z) (called even-even nucleus), beta decay will lead to an odd-odd nucleus which is less stable. For some such isotopes the beta decay is energetically forbidden. In 1935, Maria Goeppert-Mayer pointed out that they can still decay through a double beta decay process :  $(Z, A) \rightarrow (Z + 2, A) + 2e^- + 2\bar{\nu}_e + Q_{\beta\beta}$ , where the  $Q_{\beta\beta}$  is the released energy. This is called ordinary double beta decay or  $2\nu\beta\beta$ , which is allowed by the Standard Model and with a typical half-life  $T_{1/2} > 10^{19}$  years[?].

In 1937, Ettore Majorana proposed that neutral spin-1/2 particles (fermions) can be their own antiparticles[?]. If neutrinos have this behaviour, the process called neutrinoless double beta decay ( $0\nu\beta\beta$ ) will also be expected. The Feynman diagrams of  $2\nu\beta\beta$  and  $0\nu\beta\beta$  are illustrated in Figure ??.

The interpretation of the  $0\nu\beta\beta$  process is considered as exchanging light Majorana neutrinos. In this case the effective Majorana mass  $\langle m_{ee} \rangle = \sum_{i=1}^3 |U_{ei}|^2 m_i$  ( $i = 1, 2, 3$ ),  $U_{ei}$  are the elements of the neutrino mixing matrix for the flavor state  $\nu_e$ , and  $m_i$  are the mass eigenvalues of the mass eigenstates (from (2.9)). The observable quantity is the half-life :

$$(T_{1/2}^{0\nu\beta\beta})^{-1} = G_{PS}(Q, Z) |M_{Nuclear}|^2 \langle m_{ee} \rangle^2,$$

where  $G_{PS}$  is the phase space factor and  $|M_{Nuclear}|$  is the nuclear matrix element for the physics process describing the  $0\nu\beta\beta$  decay process[?].

Similar to beta decay, the  $2\nu\beta\beta$  process will cause a continuous spectrum in the detector while the  $0\nu\beta\beta$  process only has two electrons in the final state, which sum up to give a distinct energy peak. By measuring this exact energy, a detector with high energy resolution is able to search for the  $0\nu\beta\beta$  signal from the  $0\nu\beta\beta$  decay radioactive isotopes. Diverse technologies have been developed during the past decades. The following section lists some



of the mainstream experiments.

$$\Psi_R = \begin{bmatrix} \psi_R \\ \psi_R^C \end{bmatrix}, \Psi_L = \begin{bmatrix} \psi_L \\ \psi_L^C \end{bmatrix}, M = \begin{bmatrix} m_L^M & m^D \\ m^D & m_R^M \end{bmatrix}, \quad (2.11)$$

The mass eigenstates :

$$m_{\pm} = \frac{1}{2} [ (m_L^M + m_R^M) \pm \sqrt{(m_L^M - m_R^M)^2 + 4(m^D)^2} ],$$

from (2.3), there are 4 cases for discussion :

- (1) If  $m_L^M = m_R^M = 0$ ,  $m_{1,2} = m^D$ , neutrinos are pure Dirac particles.
- (2) If  $m^D \gg m_{L,R}^M$ ,  $\frac{m^D}{m_{L,R}^M} \rightarrow 0$ ,  $m_{1,2} = \frac{1}{2}m^D [ \frac{(m_L^M + m_R^M)}{m^D} + \sqrt{(\frac{m_L^M - m_R^M}{m^D})^2 + 4} ] \approx m^D$ , neutrinos are Pseudo-Dirac-Neutrinos.
- (3) If  $m^D = 0$ ,  $m_1 = m_L^M$ ,  $m_2 = m_R^M$ , neutrinos are pure Majorana particles.
- (4) In the case of the seesaw mechanism, where  $m_R^M \gg m^D$ ,  $m_L^M = 0$ , and for  $(\frac{m^D}{m_R^M})^2 \rightarrow 0$ , use  $(1+x)^\alpha \sim 1 + \alpha x$  ( if  $x \rightarrow 0$  ), we get :

$$m_1 = m_- = \frac{\frac{1}{2}[(m_R^M)^2 - (m_L^M)^2 - 4(m^D)^2]}{m_R^M(1 + \sqrt{1 + 4(\frac{m^D}{m_R^M})^2})} \approx -\frac{(m^D)^2}{m_R^M},$$

$$m_2 = m_+ = \frac{1}{2}[m_R^M + m_R^M(1 + \frac{1}{2}(\frac{2m^D}{m_R^M})^2)] = m_R^M[1 + (\frac{m^D}{m_R^M})^2] \approx m_R^M.$$

For  $\mathcal{O}(1TeV)$ , the  $\nu$  mass is 0.1 eV

### 2.3.1 Status of Double Beta Decay Experiments

At the time of writing,

$0\nu\beta\beta$  in the range of  $10^{25} - 10^{26}$  year,

The GERmanium Detector Array (GERDA) experiment searches for  $0\nu\beta\beta$  of  $^{76}\text{Ge}$ . The experiment uses bare germanium crystals with an enrichment of up to  $\sim 87\%$   $^{76}\text{Ge}$  operated in a radiopure cryogenic liquid argon (LAr). GERDA Phase I had an exposure of 21.6 kg·yr and Phase-II started with 35.6kg from enriched material in December 2015. With combined data of Phase I and Phase II,

a total exposure of 82.4 kg·yr

GERDA reported in 2019 a lower limit half-life of  $T_{1/2}^{0\nu}(^{76}\text{Ge}) > 0.9 \times 10^{26}$  years at 90% C.L.[?, 2].

The Enriched Xenon Observatory (EXO) experiment uses 200-kg liquid Xenon (LXe) time projection chamber (TPC) to search for  $0\nu\beta\beta$  in  $^{136}\text{Xe}$ . In 2011 they observed the half life of double beta decay of  $^{136}\text{Xe}$  to be  $2.11 \times 10^{21}$  years and in 2014 they set a limit on  $T_{1/2}^{0\nu}(^{136}\text{Xe}) > 1.1 \times 10^{25}$  yr[?]. EXO is now upgrading to the next 5-tonne experiment (nEXO) and is expected to reach an exclusion sensitivity of  $T_{1/2}^{0\nu}(^{136}\text{Xe})$  to about  $10^{28}$  years at 90% C.L.[?].

Also looking into  $^{136}\text{Xe}$ , the KamLAND-Zen (ZEroNeutrino) experiment exploits the existing facilities of KamLAND by setting a 3.08-m-diameter spherical inner balloon filled with 13 tons of Xe-loaded liquid scintillator at the center of the KamLAND detector.

liquid scintillator cocktail of 82% decane and 18% pseudocumene by volume, 2.7 g/L PPO.

photocathode coverage of 34%.

Their 2016 results from a 504 kg·yr exposure obtained a lower limit for the  $0\nu\beta\beta$  decay half-life of  $T_{1/2}^{0\nu}(^{136}\text{Xe}) > 1.07 \times 10^{26}$  yr at 90% C.L. and the corresponding upper limits on the effective Majorana neutrino mass are in the range 61 – 165 meV[?].

The Particle and Astrophysical Xenon Experiment III (PandaX-III) high pressure gas-phase time projection chamber (TPC)

The Cryogenic Underground Observatory for Rare Events (CUORE) experiment searches for  $0\nu\beta\beta$  in  $^{130}\text{Te}$ . CUORE is a ton-scale cryogenic bolometer array that arranges 988 tellurium dioxide ( $\text{TeO}_2$ ) crystals. CUORE reported first results in 2017 after a total  $\text{TeO}_2$  exposure of 86.3 kg·yr. An effective energy resolution of  $(7.7 \pm 0.5)$  keV FWHM and a background count of  $(0.014 \pm 0.002)$  counts/(keVkg·yr) in the ROI were achieved in that data exposure. Combined with the early data (the data from the two precursor experiments, Cuoricino and CUORE-0), they placed a lower limit of  $T_{1/2}^{0\nu}(^{130}\text{Te}) > 1.5 \times 10^{25}$  yr at 90% C.L. and  $m_{\beta\beta} < (110 - 520)$  meV[3]. In five years live time, the experiment will give a projected sensitivity of  $9.5 \times 10^{25}$  yr at the 90% C.L. and set an upper limit on the effective

Majorana mass in the range  $50 - 130$  meV[21].

## Chapitre 3

# The SNO+ Experiment

### 3.1 A Description of SNO+ Detector

#### 3.1.1 Overview

The SNO+ experiment is located at SNOLAB in Vale's Creighton mine in Sudbury, Ontario, Canada. The deep underground facility of the SNOLAB provides a  $2092 \pm 6$  m flat overburden of rock, which is  $5890 \pm 94$  water equivalent meter (w.e.m). This rock overburden ensures an extremely low rate of cosmic muons passing through the detector. The rate is  $0.27 \mu/m^2/day$ , compared to an average flux of about  $1.44 \times 10^6 \mu/m^2/day$  at sea level[1].

The detector has been running since December 2016[?],

The SNO+ detector is the successor of the SNO experiment, which makes use of the SNO detector structure.

detector consists of an acrylic vessel (AV) sphere of 12 m in diameter and

5.5 cm in thickness. The AV sphere is concentric within a stainless steel photomultiplier(PMT) support structure (PSUP), with an average radius of 8.4 m. The Hamamatsu 8-inch R1408 PMTs are mounted on the PSUP. 9394 PMTs are looking inward to the AV, giving a 50% effective coverage, while 90 PMTs are looking outward, serving as muon vetos. These two structures are housed in a rock cavity filled with 7000 tonnes of ultrapure water (UPW) to provide both buoyancy for the vessel and radiation shielding.

main upgrades from SNO to SNO+ BiPo tagging on partial fill data

### 3.1.2 SNO+ Physics Phases

The SNO+ detector is designed for multi-purpose measurements of neutrino physics. The experiment will go through three phases[?] :

#### 1. Water phase

The AV was filled with about 905 tonnes of ultra pure water (UPW). The detector has been collecting physics data since May 2017.

The main physics goal in this phase is to search for the invisible nucleon decay, which violates baryon number and is a prediction of Grand Unified Theory (GUT). In this decay mode,  $^{16}\text{O}$  decays into  $^{15}\text{O}^*$  or  $^{15}\text{O}^*$ , which de-excites and produces a  $\gamma$  ray of about 6 MeV.

During the water phase, different types of calibration runs have been taken. The detector responses, systematics and backgrounds are studied. Multiple physics analyses of solar neutrinos, reactor antineutrinos and nucleon decay are going on. The external backgrounds are also measured, which will be the same as the following two phases.

#### 2. Scintillator phase

The AV will be filled with 780 tonnes of liquid scintillator, which is a mixture of linear alkylbenzene (LAB) as a solvent and 2 g/L of 2,5-diphenyloxazole (PPO) as a fluor.

In this phase, the main physics goal is to measure low energy solar neutrinos : the CNO, pep and low energy  $^8\text{B}$  neutrinos. The pep neutrinos are mono-energetic, with  $E_\nu=1.442$  MeV and their flux is well predicted by the Standard Solar Model. A measurement of the pep neutrinos will give more information of the matter effects in neutrino oscillations[?].

The solar metallicity is the abundance of elements heavier than  $^4\text{He}$  (called “metal” elements in the context of astronomy). It is poorly constrained and the predictions from different solar models disagree with each other. A measurement of the CNO neutrinos can give the abundance of  $^{12}\text{C}$ ,  $^{13}\text{N}$  and  $^{15}\text{O}$  and can thus resolve the metallicity problem[?].

Geoneutrino, reactor antineutrino and supernova neutrino detections are additional goals.

A six-month period of scintillator filling and six to twelve months of data-taking are expected for this phase. During the filling, it is planned to operate the partially filled detector at a water level about 4.4 m for about two weeks. This partial filled transition phase is mainly aimed to understand the in-situ backgrounds of scintillator.

### 3. Tellurium loading phase

In this final phase, 0.5% natural Tellurium by mass will be loaded into the scintillator. Higher loading concentrations would be possible for a further loading plan[20]. The  $^{130}\text{Te}$  is a double beta decay isotope. The main purpose in this phase is searching for  $0\nu\beta\beta$  in  $^{130}\text{Te}$ .

## 3.1.3 Detection Principle

### Optical Cherenkov Radiation Detection

In the SNO+ water phase, the relay on the .

For any charged particle travelling in a transparent medium at an ultrarelativistic speed (a speed greater than the local phase speed of light in the medium), there is an electromagnetic radiation emitted from the medium under the action of the field of the moving particle[17].

$$v > v_p = c/n(\omega)$$

$$\cos\theta_c = (1/n\beta)$$

where  $c$  is the speed of light in vacuum,  $n$  is the refraction index of the medium and  $v = \beta c$  is the speed of the particle in the medium.

Frank-Tamm formula

For a particle with a charge of  $ze$ , the number of photons produced by Cherenkov radiation per unit path length and per unit energy interval of the photons is described by :

$$\frac{d^2N_r}{dE dx} = \frac{\alpha^2 Z^2}{\hbar c} \mu(E) \left(1 - \frac{1}{\beta^2 n(E)^2}\right)$$

where  $\alpha$  is the fine structure constant

For the case of  $e^-$  travelling in the water, we can find that 0.262 MeV is the lowest kinetic energy to create Cherenkov radiation, which is called the Cherenkov threshold.

### Scintillation Detection

prompt emission of scintillation light, which is called fluorescence  
 delayed emission of scintillation light, which is called delayed fluorescence or phosphorescence.

#### 3.1.4 Electronics

The SNO+ electronics system includes trigger and readout systems, which record the time and charge information of PMT signals. The system can measure signals with a nanosecond-level timing resolution and single-photon level charge resolution and handle a rate of several kHz for normal operations.

burst from supernova

PMTs are Hamamatsu model R1408.

a single RG59/U type 75  $\Omega$  coaxial cable

19 crates $\times$ 16 cards $\times$ 32 channels = 9728 electronics channels.

Each crate processes  $16 \times 32 = 512$  PMTs. 9605 channels are actually used and among them, 32 channels are reserved for calibration devices and labelled as FEC Diagnose (FECD) channels

During the experiment running, the maintenance of the electronics is always ongoing.

crate controller card (XL3)

analog master trigger system (MTC/A+) ("+" means an upgrade to SNO MTC/A)

digital master trigger system (MTC/D)

the analog waveforms are summed on the MTC/A+ card, then they are digitized

CAEN v1720 digitizer

TUBii trigger utility board pulsters and delays

DAQ

nearline provides a real-time analysis of the data quality,

trigger system PMT Interface Card (PMTIC) Front End Card (FEC)

NHit20 (N20), NHit100 (N100) trigger pulses.

MTC/A has 3 discriminators : LOW, MED and HI.

Global Trigger (GT) the timing and charge from the fired PMT is digitized and stored.

Nhit means the number of live hit PMTs in the detector for a given event.

dark noise rate is estimated to be 1 kHz.

### 3.1.5 Optics

Optical parameters

Winston cone

timing

attenuation

scattering

laser pulse diffuser, it can run with different wavelengths : 337, 365, 385, 420, 450 and 500 nm. The laserball

The acrylic of the AV is UV-transparent

### 3.1.6 Liquid scintillator

Linear Alkyl Benzene (LAB)

is provided by CEPSA Química Bécancour Inc. Organic liquid scintillators The advantages of LAB are :

- It has very low levels of natural radioactive contaminants such as U, Th and K.
- High light yield and attenuation length.
- It has fast timing response different timing spectrum for  $\alpha$  and  $\beta$  events, which enables an  $\alpha - \beta$  discrimination.
- High flash point and low toxicity for lab safety.
- appropriate density for mechanical stability
- Good stability and chemically compatible with detector materials, mainly the AV.



- Low cost.

Te-loaded liquid scintillator (TeLS)

To load the tellurium into the liquid scintillator, a compound is made by condensation reactions between telluric acid (TeA) and 1,2-butanediol (BD), with N,N-dimethyldodecylamine (DDA) being used as a stabilization agent.

2 g/L PPO gives an absolute light yield of 11900 photons/MeV.

for the partial-fill phase, 0.5 g/L PPO gives Measurements in 0.5 g/L showed a light yield of 52% of 2 g/L, 6190 photons/MeV[26, 13].

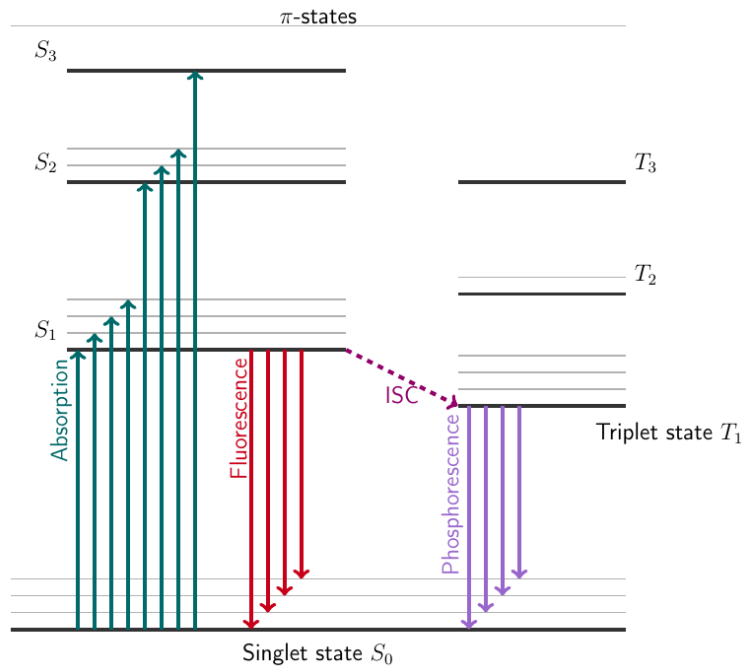


FIGURE 3.1 – A Jablonski diagram for the liquid scintillator, modified from [16, 5].

Tellurium-loaded 65% of the pure, unloaded scintillator

water-based wavelength shifter

timing profile, the intensity of scintillation light as a function of time

the prompt fluorescence intensity at a time  $t$  excitation be  $I = I_0 e^{-\frac{t}{\tau}}$

singlet and triplet states ionization density depend  $\alpha$ -particle high ionization density

quenching,

### 3.1.7 Calibration

Two kinds of calibration sources are used by SNO+ : optical sources and radioactive sources. The optical sources are used to calibrate the PMT response and to measure the optical properties of the

The radioactive sources are used to calibrate the energy reconstruction performances and uncertainties. particle identifications

Calibration sources with known physics parameters : help to understand the detector response to the events and to make accurate measurements Two types of SNO+ calibration sources : optical sources and radioactive sources Optical sources : phototube response, optical properties of the detector media Radioactive source : energy scale, resolution, systematic uncertainties  $^{16}\text{N}$  calibration source is one of the radioactive sources

Optical calibration *in-situ*

- Timing module for the Embedded LED Light Injection Entity (TELLIE)  
light-emitting diode (LED)  
time calibration, time response  
a precision of  $\mathcal{O}(1 \text{ ns})$   
Blinky fibre optics nailed to the PSUP to calibrate stuff.
- 
- 

Calibration source

The  $^{16}\text{N}$  source  $^3\text{H}(p, \gamma)^4\text{He}$  reaction.

the SNO+ Source Manipulator System (SMS) is inherited from the SNO.

A Umbilical Retrieval Mechanism (URM) is used to send the source down to the inner vessel.

The sources are connected to the umbilical.

An umbilical encloses electrical cables, optical fibres and gas lines connected to the source.

A Universal Interface (UI) connecting the URM and the detector, Therefore, sealed

environment, which ensures radon gas not leaking into the detector when deploying the source.

-

## Chapitre 4

# Event Reconstruction

### 4.1 Reconstruction of the SNO+

### 4.2 Reconstruction Algorithms for Position, Time and Energy of Events in SNO+

### 4.3 An Alternative Vertex Reconstruction Algorithm for SNO+

A Multi-path Fitter (MPF) framework was developed by the University of Alberta group as an alternative reconstruction algorithm to the SNO+ official fitter. In this framework, fitters for SNO+ water phase (MP Water Fitter), wavelength shifter (MP WLS Fitter), partial-fill phase (MP Partial Fitter) and scintillator phase (MP Scint Fitter) were developed. In SNO+ water phase, the cavity and the AV are both filled with pure water. This is a relatively simple geometry. Therefore, we start with the MP Water Fitter to explain the reconstruction concepts.

First, the fitter throws a random vertex (uniformly distributing) inside the PSUP as a trial vertex. The Class Library for High Energy Physics (CLHEP) is used for creating pseudo-random numbers.

$$rand0 = Uniform(0, 1), rand1 = Uniform(-1, 1)$$

```

double ran0 = CLHEP : :RandFlat : :shoot( 0.0, 1.0 ); double ran1 = CLHEP : :Rand-
Flat : :shoot( -1.0, 1.0 ); double ran2Pi = CLHEP : :RandFlat : :shoot( 0.0, 2.0*CLHEP : :pi
); double t = CLHEP : :RandFlat : :shoot( 100.0, 300.0 );

double wl = CLHEP : :RandFlat : :shoot( 4000.0, 6000.0 ); double r = pow(ran0,
1.0/3.0) * fPSUPRadius; // mm double costheta = ran1; double sintheta = sqrt(1.0 -
costheta*costheta);

time residual

```

$$t_{res} = t_{PMT} - t_{transit} - t_{event}$$

The MP Water Fitter uses prompt light and assumes that photons propagate in straight lines (straight light paths) for likelihood calculations. Detailed situations, such as the reflection and lensing effects from different detector components are neglected. Figure ?? shows the reconstruction concepts for position and direction.

The MPW fitter currently fits for position, time and direction of a water phase event. The fitter uses prompt light and straight line paths for likelihood calculations. Then it utilizes the Multi-path Fitter to maximize the likelihood functions and find the best-fit values. The concept of this fitter is the same of the FTU fitter in SNO time.

**MPW : Fitter Structure** The MPW fitter consists of :

- Fitter Data : Includes physics constants, set-values and pdfs for the MPW fitter.

These parameters are set in the MPW database.

- Water reflection index (water\_RI, or  $n_{water}$ ), used for group velocity ( $v_g = c/n_{water}$ ) calculation.

The MPW fitter currently uses one fixed number for  $n_{water}$ , rather than a function of wavelengths. The value of  $n_{water}$  can be tuned to give the lowest biases of the fitted positions to the Monte Carlo and to give the lowest RMS of fitted results as well. But the effect of  $n_{water}$  can also be corrected by the drive correction afterwards. Currently  $n_{water} = 1.38486$  is obtained by analyzing the time of flight from the  $^{16}\text{N}$  central run-100934 data reconstructed by the MPW fitter.

- Constants for fit setting : Includes the fitter tolerance, the maximum iterations for the Multi-path Fitter to converge, time offset, radius cut for position vertex, fitting bin-width and steps.
- Other physics constants : air reflection index (air\_RI), psup radius.
- PMT response time (timing) pdf for the position reconstruction, as shown in 4.1. The pdf shown in red line is modified from the measured PMT response time distribution from SNO time and the late light response is forced to be de-weighted (black). The pdf is modified in  $[-100, -4]$  ns region to match the time residual spectrum obtained from

FIGURE 4.1 – PMT response time as the timing pdf.

- PMT angular response pdf for the direction reconstruction, as shown in 4.2. It is taken from the Monte Carlo simulation of 5 MeV electrons traverse in the AV with one direction.

FIGURE 4.2 – PMT angular distribution as the angular response pdf.

- Fit the position, time and direction.
  - Likelihood Calculation Classes : Constructs likelihood functions, calculates likelihoods and their derivatives. For the MPW fitter, there are two classes : WaterPosition for position reconstruction and WaterDirection for direction reconstruction. The WaterPosition class tackles with 4 parameters (x,y,z,t) and the WaterDirection class tackles with 2 parameters ( $\theta, \phi$ ).
  - Multi-path Fitter : Processes the MPW fitter and finds the best-fit of the likelihood function. It is a general processor and is shared with the fitters using the Multi-path Fitter, including the MPW fitter, air-water (AW) fitter, wavelength-shifter (WLS) fitter and scint-water fitter (being developed). It processes a certain fitter by being assigned the fitter name in macro. It processes the fitter event by event : for every triggered event, it first calls PMT selectors (ModeCut or StraightTimeResidualCut) and sends the information of the reduced PMTs to a certain Likelihood Calculation

Class for likelihood calculations. The Likelihood Calculation Class sends back the values of likelihoods and their derivatives, so the Multi-path Fitter does not care about how the likelihood functions are constructed and how the likelihoods and derivatives are calculated. Using these values, it constructs an  $n \times n$  Hessian matrix ( $n$  is the number of fitting parameters defined in Likelihood Calculation Class) and uses the Levenberg-Marquardt (MRQ) method to maximize the likelihood and finds the best-fit values. For the MPW, if the likelihood maxima is found 5 times for any position and direction then values are returned as the fitted position and direction. For the MPW case, it calls the ModeCut and fits for the position and time; then it calls the StraightTimeResidualCut and fits for the directions.

- Dump Likelihood : It is a function inside the Multi-path Fitter. It stores the likelihood surfaces and their derivatives from the fitting of the Multi-path Fitter to check whether the fitter finds global or local maximum of the interested events and to check the reconstruction performances. It requires a switch on/off parameter and the GTIDs of the interested events (a list of GTIDs) from the MPW database.

- SDecompQRH : It is a fit method class modified from ROOT TDecompQRH. It is used by the Multi-path Fitter to invert the Hessian matrix. Compared to ROOT, Solve() for  $Ax=b$  is modified to zero the component of  $x$  for which the diagonal element in  $R$  is small. This allows a Levenberg-Marquardt optimization to continue in many cases when the matrix is singular. For the MPW case, it is used to invert  $4 \times 4$  matrix of the WaterPosition Class while the inversion of  $2 \times 2$  matrix of the WaterDirection is calculated directly.

- ModeCut : The same class used by Rat. Selects the PMTs of an event by a mode time window. For the MPW, the optimized window is  $[-50 + t_{mode}, 100 + t_{mode}]$  ns obtained from

- StraightTimeResidualCut : Selects the PMTs of an event by a time residue window. This selector requires a fitted position and fitted time. It calculates the time residue directly by assuming straight light path, which is the same method used by Multi-

path fitter. For the MPW case, it is used for the direction fit after the position and time are reconstructed. The default window is  $[-10, 250]$  ns.

**MPW : Position and Direction Reconstructions** For the position reconstruction of the MPW fitter, the likelihood function simply calculates the likelihood assuming straight line paths of prompt light from a position vertex  $\vec{X}_0$  (fVertex) and a starting time offset  $t_0$  to each of the hit PMTs.

The time residue ( $t_{res}$ ) is taken as the fitting parameter of the likelihood function for position reconstruction. The  $t_{res}$  of the  $i$ -th hit PMT is calculated as  $t_{res}^i = t_{pmt}^i - |\vec{X}_0 - \vec{X}_{pmt}^i|/v_g - t_0$ , where  $t_{pmt}^i$  is the hit time of the  $i$ -th hit PMT and  $\vec{X}_{pmt}^i$  (fPosition) is the position of the  $i$ -th hit PMT. Then the likelihood function for position reconstruction is constructed as :

$$L(\vec{x}_0, t_0) = \sum_{i=1}^{N_{hits}} L_i(t_{res}^i)$$

We define the position difference  $\vec{X}_{diffCh} = \vec{X}_0 - \vec{X}_{pmt}$ , then the time of flight for prompt light is  $t_{Ch} = |\vec{X}_{diffCh}|/v_g$  and  $L_{Ch} = L(t_{Ch})$ .

The derivatives of the likelihood function can be calculated from explicit mathematical forms as :

$$\frac{\partial L}{\partial t_0} = \frac{dL_{Ch}}{dt_{Ch}},$$

$$\frac{\partial L}{\partial x} = \frac{\partial L_{Ch}}{\partial t_{Ch}} \frac{dt_{Ch}}{\partial x} = -\frac{dL_{Ch}}{dt_{Ch}} \frac{X_{diffCh}}{|\vec{X}_{diffCh}| \cdot v_g},$$

$$\frac{\partial L}{\partial y} = -\frac{dL_{Ch}}{dt_{Ch}} \frac{Y_{diffCh}}{|\vec{X}_{diffCh}| \cdot v_g},$$

$$\frac{\partial L}{\partial z} = -\frac{dL_{Ch}}{dt_{Ch}} \frac{Z_{diffCh}}{|\vec{X}_{diffCh}| \cdot v_g},$$

where  $\frac{dL_{Ch}}{dt_{Ch}}$  can be calculated numerically from the timing pdf.

In the WaterPosition class, it starts with a random  $(\vec{x}_0, t_0)$  as seed and calculates the likelihoods and their derivatives for various paths. These values are sent to the Multi-path



Fitter, which is fitting 4 parameters :  $x, y, z, t$  and to maximize the likelihood function through the MRQ method and to find the best-fit positions.

For the direction reconstruction, the direction vertex  $\vec{u}_0 = (\cos \phi \sin \theta, \sin \phi \sin \theta, \cos \theta)$  (fDirection), where the  $\theta$  is zenith angle and  $\phi$  the azimuth.  $\cos \theta_{\text{Ch}}$  is the angle between  $\vec{u}_0$  and  $\vec{X}_{\text{diffCh}}$ , which is taken as the fitting parameter of the likelihood function for the direction reconstruction. For the  $i$ -th hit PMT,  $\cos \theta_{\text{Ch}}^i = \vec{u}_0 \cdot \frac{\vec{X}_{\text{diffCh}}^i}{|\vec{X}_{\text{diffCh}}^i|}$ , then the likelihood function is :

$$L(\vec{u}_0) = \sum_{i=1}^{\text{Nhits}} L_i(\cos \theta_{\text{Ch}}^i),$$

The derivatives have explicit mathematical forms :

$$\frac{\partial L}{\partial \theta} = \frac{dL_{\text{Ch}}}{d \cos \theta_{\text{Ch}}} \frac{d \cos \theta_{\text{Ch}}}{\partial \theta} = \frac{dL_{\text{Ch}}}{d \cos \theta_{\text{Ch}}} \frac{d\vec{u}_0}{d\theta} \cdot \frac{\vec{X}_{\text{diffCh}}}{|\vec{X}_{\text{diffCh}}|},$$

where  $d\vec{u}_0/d\theta = (\cos \phi \cos \theta, \sin \phi \cos \theta, -\sin \theta)$  and

$$\frac{\partial L}{\partial \phi} = \frac{dL_{\text{Ch}}}{d \cos \theta_{\text{Ch}}} \frac{d \cos \theta_{\text{Ch}}}{d\phi} = \frac{dL_{\text{Ch}}}{d \cos \theta_{\text{Ch}}} \frac{d\vec{u}_0}{d\phi} \cdot \frac{\vec{X}_{\text{diffCh}}}{|\vec{X}_{\text{diffCh}}|},$$

where  $d\vec{u}_0/d\phi = (-\sin \phi \sin \theta, \cos \phi \sin \theta, 0)$ .  $\frac{dL_{\text{Ch}}}{d \cos \theta_{\text{Ch}}}$  can be calculated numerically from the PMT angular response pdf.

In the FitterWaterDirection class, it starts with a random  $(\theta_0, \phi_0)$  as seed and calculates the likelihoods and their derivatives for various paths. These values are sent to the Multi-path Fitter, which is now fitting 2 parameters :  $(\theta, \phi)$  and to maximize the likelihood function through the MRQ method and to find the best-fit directions.

**Drive Correction** Once the MPW fitter obtains the fitted position and direction, a drive correction is applied on the fitted position by  $\vec{X}_{\text{corrected}} = p_0 \vec{X}_{\text{fit}} + p_1 \vec{u}_{\text{fit}}$ , where  $p_0$  and  $p_1$  are the correction parameters.

To obtain the values of  $p_0$  and  $p_1$ , we generated electron events distributed isotropically inside the AV. The simulations of 2, 3, 4, ... ,10 MeV electrons are produced. Then the MPW fitter is applied on each simulations and returns the results of  $\vec{X}_{\text{fit}}$  and  $\vec{u}_{\text{fit}}$ . Take the Monte Carlo generated positions  $\vec{X}_{MC}$  as the true positions, for all the fitted events, a

$\chi^2$  function is calculated by :

$$\chi^2 = \sum_{i=1}^{N_{\text{events}}} [\vec{X}_{MC}^i - (p_0 \vec{X}_{fit}^i + p_1 \vec{u}_{fit}^i)]^2$$

The  $p_0$  and  $p_1$  are obtained by minimizing the  $\chi^2$  function. When doing the  $\chi^2$  calculation, the fitted events of  $|\vec{X}_{fit} - \vec{X}_{MC}| > 3 \text{ m}$  are thrown away to improve the  $\chi^2$  minimization results.

For the 2 to 10 MeV electrons simulations, the obtained values of  $p_0$  and  $p_1$  are energy or  $N_{hit}$  dependent. However, it does not improve the results if using the  $N_{hit}$  dependent functions  $p_0(N_{hit})$  and  $p_1(N_{hit})$  as drive corrections. Finally we take the average values from the 5 to 10 MeV electrons simulations and the drive correction is set as  $\vec{X}_{corrected} = 0.995765 \vec{X}_{fit} + -63.826 \vec{u}_{fit}$ .

It is important to note that since the drive correction parameters are obtained from the reconstructions of Monte Carlo, it depends on the Monte Carlo and the results of reconstruction. Therefore, the  $n_{water}$ , mode cut and time residue cut affecting the fitted results will also affect the drive correction parameters, but not significantly.

By fitting the simulations of 5 MeV electrons generated at the detector center and travelling along +X direction, the drive effect of the MPW fitter causes a  $\sim 50$  mm biases from the detector center along +X axis. The drive correction reduces this drive bias down to  $\sim 0.2$  mm. For the reconstruction of  $^{16}\text{N}$  data, the drive correction can reduce the fitted position RMS by  $\sim 20$  mm.

## 4.4 Likelihood Calculation

to fit the nonlinear model for multiple parameters, Levenberg-Marquardt method is used.

Taylor series expansion

$$\chi^2(\theta) \approx \chi^2(\theta_{current}) + \sum_k \frac{\partial \chi^2(\theta_{current})}{\partial \theta_k} \delta \theta_k + \frac{1}{2} \sum_{\alpha\beta} \frac{\partial^2 \chi^2(\theta_{current})}{\partial \theta_\alpha \partial \theta_\beta} \delta \theta_\alpha \delta \theta_\beta$$

where

$$\kappa_{\alpha\beta} \equiv \frac{1}{2} \frac{\partial^2 \chi^2(\theta_{current})}{\partial \theta_\alpha \partial \theta_\beta}$$

is defined as the curvature matrix[12].

## 4.5 $^{16}\text{N}$ test

The  $^{16}\text{N}$  calibration runs provide an ideal test of fitter performance. From a comparison of reconstructions for data and MC, we can also extract the resolution and bias of the fitter.

The  $\gamma$  rays emitted from the  $^{16}\text{N}$  source interact with the water in the detector mainly via Compton scattering. Figure ?? shows the spatial distributions of the first  $\gamma$ -ray interaction positions projected on the x axis (called spatial distribution  $S(x)$ ) obtained from MC simulation. The  $^{16}\text{N}$  source is considered as an electron source with a known spatial distribution[?]. For simplicity, in the following we always discuss the  $x$  component of the position vector  $\vec{X}$ .

A position resolution function is defined for the reconstructed electron position distribution[?] :

$$R(x) = \frac{1 - \alpha_e}{\sqrt{2\pi}\sigma_p} \exp\left[-\frac{1}{2}\left(\frac{x - \mu_p}{\sigma_p}\right)^2\right] + \frac{\alpha_e}{2\tau_p} \exp\left[-\frac{|x - \mu_p|}{\tau_p}\right],$$

where  $\alpha_e$  is the fractional exponential component,  $\sigma_p$  is the Gaussian width (corresponding to the position resolution),  $\mu_p$  is the Gaussian shift (corresponding to the position bias) and  $\tau_p$  is the exponential slope (corresponding to the position distributions in tails).

For electrons from the  $^{16}\text{N}$  calibration source, their spatial distribution function  $N_R(x)$  can be described by the position resolution function smeared by the convolution of  $S(x)$  as[?] :

$$N_R(x) = \int_{-\infty}^{+\infty} S(x) R(x_{fit} - x) dx.$$

Since the  $S(x)$  and  $N_R(x)$  are histograms obtained from the data and MC, we calculate by the bin value  $x_i$  :

$$N_R(x_i) = \sum_{x_i=-\infty}^{+\infty} S(x_i) R(x_{fit}^i - x_i).$$

The  $\chi^2$  is calculated by :

$$\chi^2 = \sum_{i=0}^{N_{bins}} \left[ \frac{N_R(x_{fit}^i) - N_R^{fit}(x_{fit}^i)}{\sigma_i} \right]^2,$$

where  $N_R^{fit}$  is a trial fit to the  $N_R$  by tuning the  $\{\alpha_e, \mu_p, \sigma_p, \tau_p\}$  and  $\sigma_i$  is taken as the bin width of the histograms.

By minimizing the  $\chi^2$ , the parameters of the resolution function,  $\{\alpha_e, \mu_p, \sigma_p, \tau_p\}$  and a best  $N_R^{fit}$  are obtained.

Figure ?? shows a comparison of the reconstructed x position of  $^{16}\text{N}$  events between data and MC. The reconstructed position distributions are fitted with  $N_R^{fit}$ .

Table 4.1 summarizes the values of position resolution parameters obtained from data and MC of  $^{16}\text{N}$  calibration runs at the detector center.

TABLE 4.1 – Position resolution parameters for the MP Water Fitter.

MPW fitter	$\alpha_e$	$\sigma_P$ (mm)	$\tau_P$ (mm)	$\mu_P$ (mm)
data	$0.58 \pm 0.04$	$175.8 \pm 3.8$	$288.0 \pm 5.7$	$-28.8 \pm 1.0$
MC	$0.51 \pm 0.05$	$195.2 \pm 3.3$	$298.4 \pm 6.1$	$-10.9 \pm 1.0$

Vertex likelihood surface for an typical  $^{16}\text{N}$  event (calibration run-100934\_s000\_p001, event GTID = 61836), projected on X-Y, X-Z and Y-Z planes. A clean global maxima gives the reconstructed vertex : the fitted position is at  $(-211.958, 503.399, 275.990)$  mm and the fitted time at 217.03885 ns. This is shown in Fig. 4.3.

## 4.6 Vertex Reconstruction for the SNO+ Partial-phase

For the partial-phase geometry, the SNO+ acrylic vessel can be considered as composed of the neck (cylinder), AV sphere and water-scintillator interface (plane). The ray coming from the vertex to the PMT can intersect with these three geometries.

line-sphere intersection and line-plane intersection

$a_1, a_2$  and  $a_3$

trial position  $\vec{X}_0 = (x_0, y_0, z_0)$ , PMT position  $\vec{X}_{\text{pmt}} = (x_{\text{pmt}}, y_{\text{pmt}}, z_{\text{pmt}})$

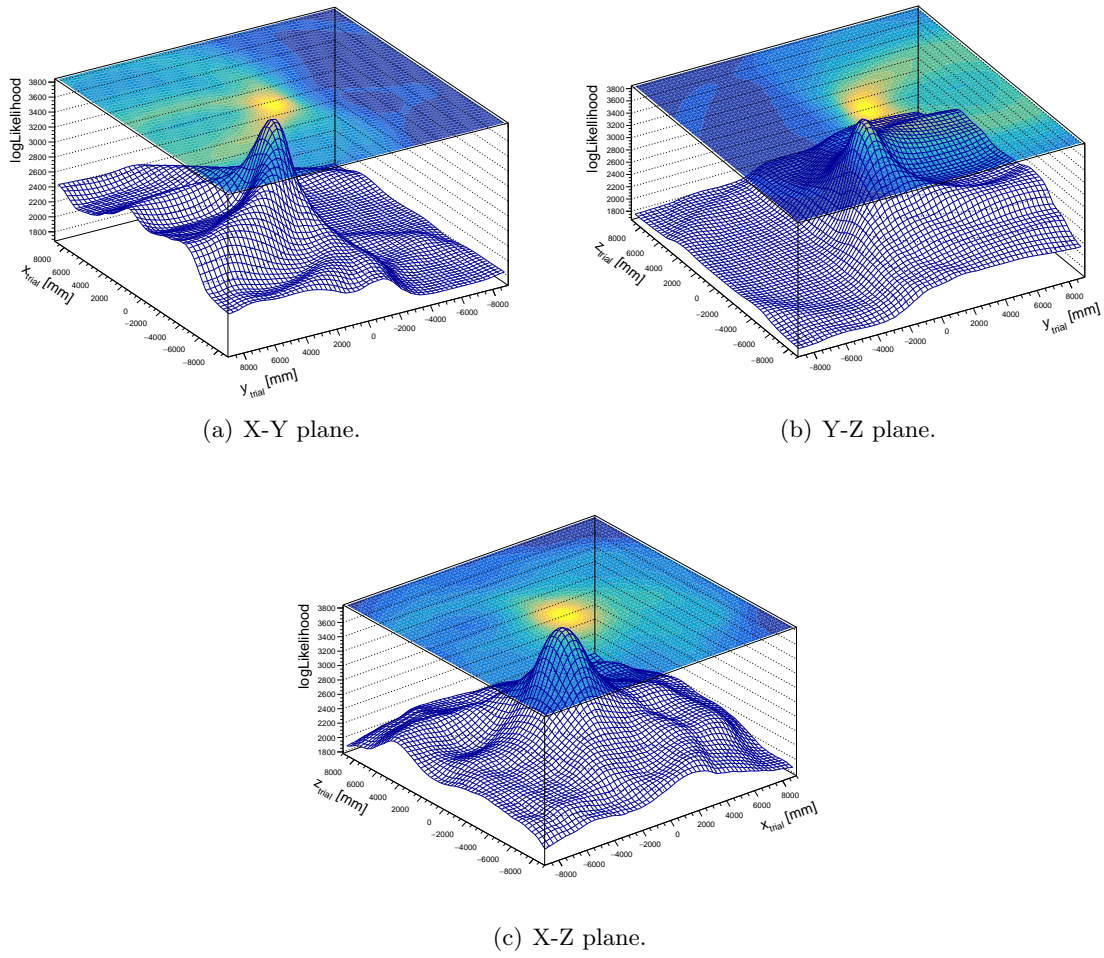


FIGURE 4.3 – Likelihood surface of an  $^{16}\text{N}$  event projected on X-Y, Y-Z, X-Z planes. A clear global maxima is reached for the fitted vertex.

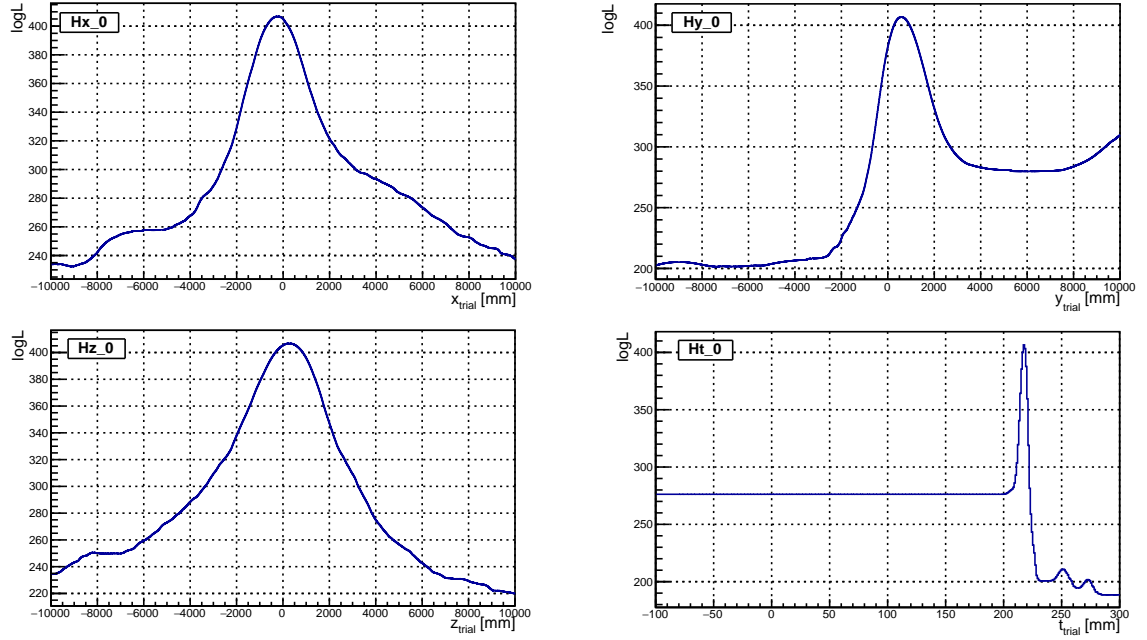


FIGURE 4.4 – Likelihood surface of an  $^{16}\text{N}$  event projected on  $x$ ,  $y$ ,  $z$ ,  $t$  axes.

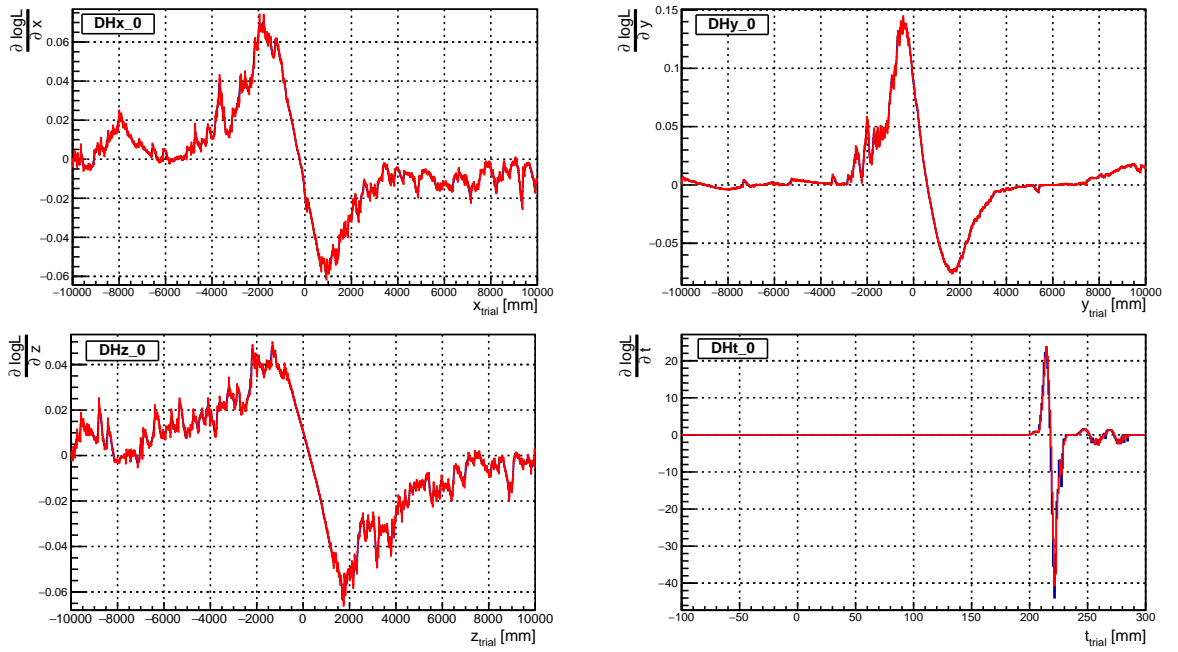


FIGURE 4.5 – Derivatives of  $\log\text{Likelihood}$  of an  $^{16}\text{N}$  event projected on  $x$ ,  $y$ ,  $z$ ,  $t$  axes. The analytical derivatives (blue) are overlaid with numerical derivatives.

ray-vector  $\vec{l}_0 = \vec{X}_0 + a \cdot \vec{u}$ , where  $a$  is the distance between vertex and intersection point. It is the parameter to be determined.  $\vec{u} = (\vec{X}_{\text{pmt}} - \vec{X}_0)$  is the direction of the ray-vector/light path.

$\vec{O}_{av}$  is the origin of the AV sphere. In the PSUP coordinate,  $\vec{O}_{av} = (0, 0, 108) \text{ mm}$ . For the ray-sphere intersection,  $(\vec{l}_0 - \vec{O}_{av})^2 = r_{av}^2$

To solve this equation, let  $\Delta = [(\vec{X}_0 - \vec{O}_{av}) \cdot \vec{u}]^2 - (\vec{X}_0 - \vec{O}_{av})^2 + r_{av}^2$  then

$$a_{+,-} = -(\vec{X}_0 - \vec{O}_{av}) \cdot \vec{u} \pm \sqrt{\Delta}, \text{ if } \Delta > 0$$

if  $\Delta \leq 0$ , there is no intersection point or only one intersection point at the AV, the ray never passes through the AV sphere.

For the ray-plane intersection,  $l_{0,z} = Z_{split}$ , where  $Z_{split}$  is the water level. If  $u_z = z_{\text{pmt}} - z_0 = 0$ , the ray is parallel to the plane and never intersects the plane. To solve this equation, we have  $a = (Z_{split} - z_0)/u_z = (Z_{split} - z_0)$ , if  $u_z \neq 0$ . Let :

$$a_3 \equiv a = \frac{(Z_{split} - z_0)|\vec{X}_{\text{pmt}} - \vec{X}_0|}{z_{\text{pmt}} - z_0} \quad (\text{if } z_{\text{pmt}} - z_0 \neq 0),$$

For the ray-cylinder intersection,  $l_{0,x}^2 + l_{0,y}^2 = r_{neck}^2$ , where  $r_{neck}$  is the radius of the neck cylinder.

$$\text{time of flight (tof)} = (a_+ - a_3)/v_{gr,scint} + [|\vec{X}_{\text{pmt}} - \vec{X}_0| - (a_+ - a_3)]/v_{gr,water}$$

$$\frac{\partial L}{\partial splitZ} = \frac{\partial L}{\partial tof} \cdot \frac{\partial tof}{\partial splitZ} = \frac{\partial L}{\partial tof} \cdot \frac{\partial a_3}{\partial splitZ}$$

$$\frac{\partial L}{\partial splitZ} = 0$$

the optical response of the liquid scintillator

empirical model. This model consists  $n$  ( $n = 3$  or  $4$ ) exponential decays with a common rise time [4].

timing profile

scintillator timing

$$\sum_{i=1}^n A_i \cdot \frac{e^{-\frac{t}{\tau_i}} - e^{-\frac{t}{\tau_{rise}}}}{\tau_i - \tau_{rise}}$$

$$\left\{ \sum_{i=1}^n A_i \cdot \frac{e^{-\frac{t}{\tau_i}} - e^{-\frac{t}{\tau_{rise}}}}{\tau_i - \tau_{rise}} * f_{PMT}(t - t') \right\} * Gaus(t, 0)$$

from bench top measurement, while the rise time,  $t_{rise} = 0.8 \text{ ns}$  the timing parameters  $t_i$ , amplitude  $a_i$  are determined by the benchtop measurements

TABLE 4.2 – scintillator  $\alpha/\beta$  timing parameters??.

scintillator	timing [ns]				amplitudes			
particles	$t_1$	$t_2$	$t_3$	$t_4$	$a_1$	$a_2$	$a_3$	$a_4$
LAB + 2g/L PPO (default scintillator)								
$e^-$	4.88	15.4	66.0	400	0.665	0.218	0.083	0.0346
$\alpha$	4.79	18.4	92.0	900	0.427	0.313	0.157	0.1027
LAB + 0.5g/L PPO (partial-fill phase)								
$e^-$	7.19	24.81	269.87	–	0.553	0.331	0.116	–
$\alpha$	6.56	23.82	224.19	–	0.574	0.311	0.115	–
LAB + 2g/L PPO + 0.5% molar concentrations DDA								
$e^-$	5.0	12.1	33.3	499.0	0.68	0.21	0.07	0.04
$\alpha$	3.8	11.3	65.3	758.0	0.48	0.32	0.14	0.06
LAB + 2g/L PPO + 0.5% molar concentrations Te+0.5% molar DDA								
$e^-$	3.7	10.0	52.0	500.0	0.72	0.23	0.02	0.03
$\alpha$	3.69	15.5	79.3	489.0	0.63	0.23	0.07	0.07

pdfs

Radial bias is defined as the difference between the fitted and true position, projected along the radial component (unit vector) of the true position [7].

$$(\vec{X}_{fit} - \vec{X}_{true}) \cdot \hat{X}_{true}$$

The value of the mean radial bias is taken by fitting the histogram of the distributions of radial biases with a Gaussian profile and then get the mean of the fitted Gaussian profile.

Appendix : Levenberg-Marquardt method for fitter minimization (ref : press2007numerical)

for M unknown parameters :  $a_0, a_1, \dots, a_{M-1}$  (for example, the 4 parameters of an event vertex :  $(x, y, z, t)$ )



the  $\chi^2$  function can be expanded and well approximated as

$$\chi^2(\mathbf{a}) \simeq \gamma - \mathbf{d} \cdot \mathbf{a} + \frac{1}{2} \mathbf{a} \cdot \mathbf{D} \cdot \mathbf{a},$$

$$\mathbf{a}_{min} = \mathbf{a}_{cur} + \mathbf{D}^{-1} \cdot [-\nabla \chi^2(\mathbf{a}_{cur})]$$

for a fudge factor  $\lambda$ ,

$$\delta a_l = \frac{1}{\lambda \alpha_{ll}} \beta_l \quad (\alpha_{ll} > 0),$$

$$\sum_{l=0}^{M-1} \alpha'_{kl} \delta a_l = \beta_k$$

Let  $\alpha \equiv \frac{1}{2} \mathbf{D}$ , which is the half Hessian, or called as curvature matrix.

$$\beta_k = -\frac{1}{2} \frac{\partial \chi^2}{\partial a_k}, \quad \alpha_{kl} = \frac{1}{2} \frac{\partial^2 \chi^2}{\partial a_k \partial a_l}$$

by optimizations, the values of tolerance, are set to .

## 4.7 PMT Selectors

- Straight Light Path TimeResidual Cut

This selector is used for the direction reconstruction for the water phase.

- Mode cut

- Early Hit PMT Selector

in prompt light time window

- Uniform PMT Selector Pick up the PMTs uniformly and

reduce the number of PMTs to a designated number to boost up the fit speed.

water phase fit speed for vertex reconstruction : 0.0017 s/call fit speed for direction reconstruction : 0.0004 s/call

## 4.8 $^{16}\text{N}$ Calibration

During the water phase, an Nitrogen-16 ( $^{16}\text{N}$ ) calibration source was deployed for internal detector calibration scans in June and November, 2017 and external detector scans in

March, 2018.

emit  $\gamma$ -rays. These  $\gamma$ -rays will Compton scatter off electrons and the electrons will emit Cherenkov light to be detected by the PMTs.

#### 4.8.1 Water Phase Calibration

#### 4.8.2 Partial-fill Phase Calibration

water level was at 5100 mm from the center of the AV (in AV coordination). LAB with a PPO concentration of 0.53 g/L

Effect of the water level.

The  $^{16}\text{N}$  source was deployed in the external water region during the partial-fill phase. run 251748 2019/09/19 and

Source position was at  $(-1120.8, 1041.4, 6172.5)$  mm for a 30-minute duration and at  $(-1120.8, 1041.4, 6108.0)$  mm for a 7-hour duration (separated into 7 runs).

## Chapitre 5

# Partial-filled Scintillator Phase

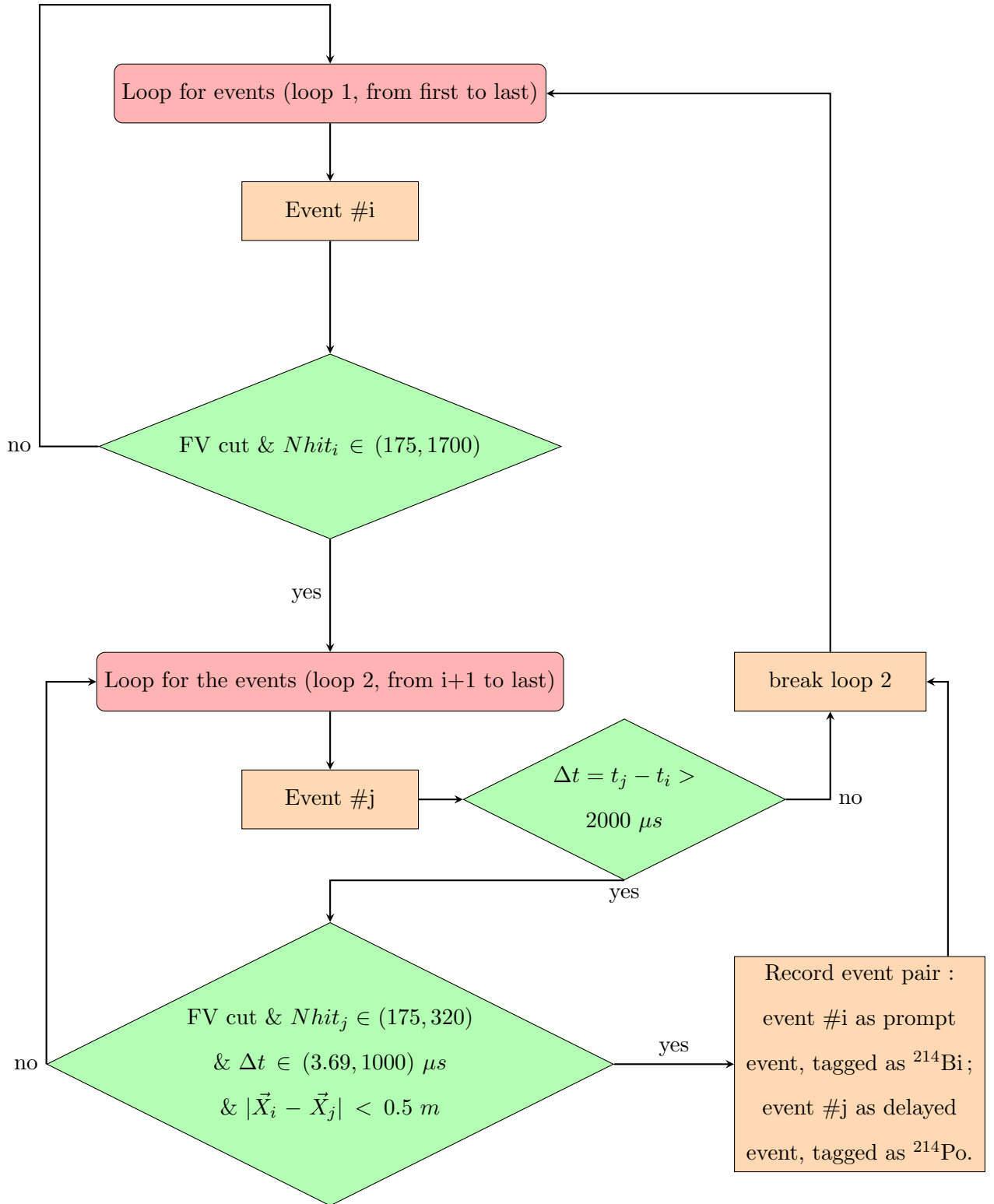
During the August to October 2019, the PPO is added into the LAB when the water level at 5100 mm (in PSUP coordinate). This is for the SNO+ partial-fill phase.

$\beta_{14}$  isotropy classifier

$$\beta_l = \frac{2}{N(N-1)} \sum_{i=1}^{N-1} \sum_{j=i+1}^N P_l(\cos \theta_{ij})$$

where  $P_l(\cos \theta_{ij})$  are Legendre polynomials

$$\beta_{14} = \beta_1 + 4\beta_4$$



$$\phi = \hat{v}_e \cdot \hat{v}_{assume}$$

$$\vec{n} = \hat{v}_e \times \hat{v}_{assume}$$

$$R = \begin{bmatrix} n_x^2(1 - \cos \phi) + \cos \phi & n_x n_y(1 - \cos \phi) - n_z \sin \phi & n_x n_z(1 - \cos \phi) + n_y \sin \phi \\ n_x n_y(1 - \cos \phi) + n_z \sin \phi & n_y^2(1 - \cos \phi) + \cos \phi & n_y n_z(1 - \cos \phi) - n_x \sin \phi \\ n_x n_z(1 - \cos \phi) - n_y \sin \phi & n_y n_z(1 - \cos \phi) + n_x \sin \phi & n_z^2(1 - \cos \phi) + \cos \phi \end{bmatrix}$$

$$\vec{v}'_e = R\vec{v}_e$$

$$\vec{X}'_{evt} = R\vec{X}_{evt}$$

Move  $\vec{X}'_{evt}$  to the origin,

$$\vec{X}'_{pmt} = R\vec{X}_{pmt} - \vec{X}'_{evt}$$

Breit-Wigner function

$$p(x) = \frac{c_0}{\pi} \frac{\frac{1}{2}\Gamma}{(x - m)^2 + (\frac{1}{2}\Gamma)^2} + c_1$$

## Chapitre 6

## Conclusions

**Annexe A**

**Appendix Name**

# Bibliographie

- [1] Muons. [https://cosmic.lbl.gov/SKliewer/Cosmic\\_Rays/Muons.htm](https://cosmic.lbl.gov/SKliewer/Cosmic_Rays/Muons.htm), 2001. [Online; accessed 19-July-2019].
- [2] M. Agostini, A. Bakalyarov, M. Balata, I. Barabanov, L. Baudis, C. Bauer, E. Bellotti, S. Belogurov, A. Bettini, L. Bezrukov, et al. Probing majorana neutrinos with double- $\beta$  decay. *Science*, page eaav8613, 2019.
- [3] C. Alduino, F. Alessandria, K. Alfonso, E. Andreotti, C. Arnaboldi, F. Avignone III, O. Azzolini, M. Balata, I. Bandac, T. Banks, et al. First results from cuore : A search for lepton number violation via  $0\nu\beta\beta$  decay of te-130. *Physical review letters*, 120(13) :132501, 2018.
- [4] S. D. Biller, E. J. Leming, and J. L. Paton. Slow fluors for highly effective separation of cherenkov light in liquid scintillators. *arXiv preprint arXiv :2001.10825*, 2020.
- [5] J. Birks and F. Firk. The theory and practice of scintillation counting. *Physics Today*, 18 :60, 1965.
- [6] M. G. Boulay. Direct evidence for weak flavour mixing with the sudbury neutrino observatory. 2004.
- [7] I. T. Coulter. *Modelling and reconstruction of events in SNO+ related to future searches for lepton and baryon number violation*. PhD thesis, University of Oxford, 2013.
- [8] P. B. Denton, S. J. Parke, and X. Zhang. Eigenvalues : The rosetta stone for neutrino oscillations in matter. *arXiv preprint arXiv :1907.02534*, 2019.



- [9] J. Dunger. *Topological and time based event classification for neutrinoless double beta decay in liquid scintillator*. PhD thesis, University of Oxford, 2018.
- [10] M. Fukugita and T. Yanagida. *Physics of Neutrinos : and Application to Astrophysics*. Springer Science & Business Media, 2013.
- [11] A. Giaz. Status and perspectives of the junos experiment. *arXiv preprint arXiv :1804.03575*, 2018.
- [12] P. Gregory. *Bayesian Logical Data Analysis for the Physical Sciences : A Comparative Approach with Mathematica® Support*. Cambridge University Press, 2005.
- [13] T. Kaptanoglu. Measurements of light yield and timing of 0.5 g/l lab+ppo. *SNO+ Internal Document, docDB-5997-v1*.
- [14] T. Kaptanoglu. Characterization of the hamamatsu 8 r5912-mod photomultiplier tube. *Nuclear Instruments and Methods in Physics Research Section A : Accelerators, Spectrometers, Detectors and Associated Equipment*, 889 :69–77, 2018.
- [15] K. Kimura, A. Takamura, and H. Yokomakura. Exact formula of probability and cp violation for neutrino oscillations in matter. *Physics Letters B*, 537(1-2) :86–94, 2002.
- [16] G. F. Knoll. *Radiation detection and measurement*. John Wiley & Sons, 2010.
- [17] L. D. Landau, J. Bell, M. Kearsley, L. Pitaevskii, E. Lifshitz, and J. Sykes. *Electrodynamics of continuous media*, volume 8. elsevier, 2013.
- [18] P. Mekarski. Electron antineutrinos in the water phase of the sno+ experiment. 2018.
- [19] B. A. Moffat. *The optical calibration of the Sudbury Neutrino Observatory*. PhD thesis, Ph. D. thesis, Queens University, 2001.
- [20] J. Paton. Neutrinoless Double Beta Decay in the SNO+ Experiment. In *Prospects in Neutrino Physics (NuPhys2018) London, United Kingdom, December 19-21, 2018*, 2019.
- [21] G. Piperno. Dark matter search with the cuore-0 experiment. 2015.
- [22] W. H. Press, S. A. Teukolsky, W. T. Vetterling, and B. P. Flannery. *Numerical recipes 3rd edition : The art of scientific computing*. Cambridge university press, 2007.

- [23] A. Y. Smirnov. The msw effect and matter effects in neutrino oscillations. *Physica Scripta*, 2005(T121) :57, 2005.
- [24] A. Y. Smirnov. Solar neutrinos : Oscillations or no-oscillations? *arXiv preprint arXiv :1609.02386*, 2016.
- [25] M. Tanabashi, K. Hagiwara, K. Hikasa, K. Nakamura, Y. Sumino, F. Takahashi, J. Tanaka, K. Agashe, G. Aielli, C. Amsler, et al. Review of particle physics. *Physical Review D*, 98(3) :030001, 2018.
- [26] J.-S. Wang. Bipo analysis using partial fill data. *SNO+ Internal Document, docDB-5950-v3*.
- [27] C. Weinheimer. Neutrino mass from triton decay. *Progress in Particle and Nuclear Physics*, 57(1) :22–37, 2006.
- [28] Z. Xing and S. Zhou. *Neutrinos in particle physics, astronomy and cosmology*. Springer Science & Business Media, 2011.
- [29] Y. Xing-Chen, Y. Bo-Xiang, Z. Xiang, Z. Li, D. Ya-Yun, L. Meng-Chao, D. Xue-Feng, Z. Xuan, J. Quan-Lin, Z. Li, et al. Preliminary study of light yield dependence on lab liquid scintillator composition. *Chinese Physics C*, 39(9) :096003, 2015.
- [30] H. W. Zaglauer and K. H. Schwarzer. The mixing angles in matter for three generations of neutrinos and the msw mechanism. *Zeitschrift für Physik C Particles and Fields*, 40(2) :273–282, 1988.
- [31] K. Zuber. On the physics of massive neutrinos. *Physics Reports*, 305(6) :295–364, 1998.